POSSIBLE AGN SHOCK HEATING IN THE COOL-CORE GALAXY CLUSTER ABELL 478

Alastair J. R. Sanderson,[1] Alexis Finoguenov,[2] and Joseph J. Mohr[1,3]

ABSTRACT

We present a detailed X-ray study of the intracluster medium (ICM) of the nearby cool-core galaxy cluster Abell 478 ($z = 0.088$), based on *Chandra* and *XMM-Newton* observations. Using a wavelet-smoothing hardness analysis, we derive detailed temperature maps of A478, revealing a surprising amount of temperature structure for an apparently well-relaxed cluster. We find the broadband *Chandra* spectral fits yield temperatures that are significantly hotter than those obtained with *XMM-Newton*, but the Fe ionization temperature shows good agreement. We show that the temperature discrepancy is slightly reduced when comparing spectra from regions selected to enclose nearly isothermal gas. However, by simulating multitemperature spectra and fitting them with a single-temperature model, we find no significant difference between *Chandra* and *XMM-Newton*, indicating that nonisothermality cannot fully explain the discrepancy. We have discovered four hot spots located between 30 and 50 kpc from the cluster center, where the gas temperature is roughly a factor of 2 higher than in the surrounding material. We estimate the combined excess thermal energy present in these hot spots to be $(3 \pm 1) \times 10^{59}$ ergs. The location of and amount of excess energy present in the hot spots are suggestive of a common origin within the cluster core, which hosts an active galactic nucleus. This cluster also possesses a pair of X-ray cavities coincident with weak radio lobes, as reported in a previous analysis, with an associated energy of less than 10% of the thermal excess in the hot spots. The presence of these hot spots could indicate strong-shock heating of the intracluster medium from the central radio source, one of the first such detections in a cool-core cluster. Using the high resolution of *Chandra*, we probe the mass distribution in the core and find it to be characterized by a logarithmic slope of -0.35 ± 0.22, which is significantly flatter than an NFW (Navarro, Frenk, and White) cusp of -1 and consistent with recent strong-lensing results for a number of clusters.

Subject headings: cosmology: observations — galaxies: active — galaxies: clusters: general — galaxies: clusters: individual (A478) — X-rays: galaxies: clusters

1. INTRODUCTION

Clusters of galaxies are critical sites for investigating the interaction between galaxies and their environment, particularly their impact on the gaseous intracluster medium (ICM). There is substantial evidence to demonstrate that the ICM has been subjected to nongravitational heating and/or cooling, so as to break the simple, self-similar scaling of cluster properties with mass; e.g., the L-T_X (e.g., Edge & Stewart 1991; Arnaud & Evrard 1999; Fairley et al. 2000), M_{gas}-T_X (Mohr et al. 1999), and isophotal size–temperature (Mohr & Evrard 1997) relations. Furthermore, it is apparent that the ICM is systematically underdense and more extended in less massive halos (e.g., Ponman et al. 1999; Sanderson et al. 2003; Osmond & Ponman 2004; Afshordi et al. 2005) and that there is an increasing excess of entropy in the gas in cooler systems (Ponman et al. 2003).

While these observations can be explained by the impact of feedback associated with galaxy formation (e.g., Voit & Ponman 2003), the precise details of the mechanisms that mediate this interaction remain unknown. Of critical importance is the role of radiative cooling, which could fuel star formation and gradually deplete the reservoir of gas in the cluster core. Despite the inherently unstable nature of cooling by thermal bremsstrahlung, gas in the dense, undisturbed cores of galaxy clusters does not appear to be cooling at the expected level (e.g., Tamura et al. 2001; Peterson et al. 2003; Kaastra et al. 2004), leading to greatly

reduced mass deposition rates (Makishima et al. 2001; Böhringer et al. 2002). A plausible explanation for this behavior is that thermal conduction acts to transfer significant amounts of energy from the outer regions of the ICM (Kim & Narayan 2003; Voigt & Fabian 2004). However, this process cannot operate at all (Khosroshahi et al. 2004) or effectively enough (e.g., Wise et al. 2004) to heat the core in all cases, especially at lower temperatures.

Since many "cooling flow" clusters are known to harbor central radio sources (Burns 1990; Eilek 2004), it is likely that active galactic nuclei (AGNs) can deposit energy directly into the ICM and thus offset at least some of the cooling. Recently, Croston et al. (2005) have demonstrated that heating from low-power radio galaxies could account for the steepening of the L-T_X relation in X-ray–bright galaxy groups. Although clusters are much more massive, the amount of energy output by powerful radio sources is certainly sufficient to heat the gas by the required amount (Churazov et al. 2002); what is lacking is a clear understanding of exactly how this energy is coupled to the ICM.

A number of clusters have been shown to possess cavities, where expanding radio lobes have displaced the ambient medium and left a depression in the projected X-ray surface brightness (e.g., see the compilation of Bîrzan et al. [2004] and references therein). However, the coolest gas is generally found beside these lobes (Fabian et al. 2000; McNamara et al. 2001), and their essentially subsonic expansion is not obviously heating the ICM by a significant amount. In the meantime, the role of AGN-driven bubbles in modifying the ICM is opening up as a very promising avenue of research (see Gardini & Ricker [2004] for a recent review).

Alternatively, energy may be transferred to the ICM by means of acoustic waves generated by turbulence (Fujita et al. 2004) or viscous dissipation of sound waves originating from a central

[1] Department of Astronomy, 1002 West Green Street, University of Illinois, Urbana, IL 61801-3080; ajrs@astro.uiuc.edu.
[2] Max-Planck-Institut für extraterrestrische Physik, Giessenbachstrasse, 85748 Garching, Germany.
[3] Department of Physics, 1110 West Green Street, University of Illinois, Urbana, IL 61801-3080.

radio source (Ruszkowski et al. 2004a, 2004b). Fabian et al. (2003) have recently discovered ripples in the X-ray emission from the Perseus Cluster, which point to a continuous energy output from the central radio source that can balance cooling within the innermost 50 kpc of the core.

In this paper we examine in detail the properties of the ICM in a nearby galaxy cluster, using X-ray data from two different telescopes. This apparently well-relaxed system has a large cool core, and its central galaxy hosts an active radio source, affording an excellent opportunity to study its interaction with the ICM. We assume the following cosmological parameters: $H_0 = 70 \, \mathrm{km \, s^{-1} \, Mpc^{-1}}$, $\Omega_m = 0.3$, and $\Omega_\Lambda = 0.7$. Correspondingly, at our adopted redshift for A478 of 0.088, $1'' = 1.65$ kpc. Throughout our spectral analysis we have used XSPEC version 11.3.0, incorporating the default solar abundance table of Anders & Grevesse (1989). All errors are $1 \, \sigma$ unless otherwise stated.

2. DATA REDUCTION

2.1. *Chandra X-Ray Data Reduction*

A 42.4 ks *Chandra* observation of Abell 478 was made on 2001 January 29 using the Advanced CCD Imaging Spectrometer (ACIS) in FAINT mode. The data reduction and analysis were performed with CIAO version 3.0.2 and CALDB version 2.26. This release of the *Chandra* CALDB calibration files was the first to incorporate a full correction for the degradation in quantum efficiency of the ACIS detectors. Therefore, no further steps were taken to correct for its effects.

Three separate light curves were constructed for the S1, the S3, and the remaining CCDs combined, using the recommended energy and time-binning criteria.[4] A small flare was identified in the light curve from the S1 CCD, and another was found in the combined I2, I3, S2, and S4 light curve: both were excluded, leaving 40.7 ks of useful data. Only events with *Advanced Satellite for Cosmology and Astrophysics* (*ASCA*) grades 0, 2, 3, 4, and 6 were used, and bad columns and hot pixels were excluded. In addition, those events associated with cosmic-ray afterglows were identified and removed. A correction was applied to the level 1 events file to allow for the ACIS time-dependent gain variation, using the tool[5] `corr_tgain`, and a new level 2 events file was generated by reprocessing this modified level 1 events data set.

Since A478 fills much of the *Chandra* field of view, we use the Markevitch blank-sky data sets to estimate the background contribution.[6] To allow for small variations in the particle background level between the blank-sky fields and the A478 observation, we rescaled the effective exposure of the background data sets according to the ratio of count rates in the particle-dominated 7–12 keV energy band for the S1 CCD, which is farthest away from the cluster. To avoid the bias caused by contaminating point sources in the A478 data set, we identified and excluded such features using the following iterative scheme.

Images were extracted in the 0.5–2.0 keV band for the S1 CCD in both the main (A478) and blank-sky data sets. A background image was created by smoothing the blank-sky field with a Gaussian of width $1'$ to filter out Poisson noise. The main image was then searched for sources with the CIAO task `wavdetect`, using this background. The source regions found were then masked out of both the main and blank-sky data sets, and the remaining counts in the 7–12 keV band were summed. A rescale factor was

then determined as the ratio of the net count rate in the background data set to that in the main data set. The effective exposure time of the blank-sky data set was then multiplied by this rescale factor and the process repeated, until no new source regions were found. A total of six contaminating source regions were identified and excluded from the S1 CCD data in this way. We found that the blank-sky data were 8% higher than those in the A478 observation, consistent with the value of 10% quoted by Sun et al. (2003, hereafter S03) for the same observation.

2.2. *XMM-Newton X-Ray Data Reduction*

XMM-Newton observed A478 in orbit 401 (ObsID 0109880101), using the thin filter to block visible light. In the analysis that follows, we present the data obtained with the pn CCD camera (Strüder & et al. 2001), operated in extended full-frame mode, with an exposure time of 42 ks. The initial stages of the data reduction were performed using XMMSAS version 5.4.1. Screening the data for contamination from flares was achieved by examining a light curve of detector counts in the 10–15 keV band. We have adopted the approach that is based on the analysis of the count rate histogram, as described in Zhang et al. (2004), which is more sensitive to the background conditions during the observations than using a fixed threshold to identify good time intervals.

With these screened photon event files we produced a pn image of A478 in the energy bands 0.5–2.0 and 2.0–7.5 keV. In the imaging analysis, we included photons near the pn CCD borders, those near bad pixels and offset columns, in order to reduce the width of the gaps between CCD chips. This is a reasonable approach to adopt when dealing with qualitative images in broad energy bands. For the spectral fitting, described in § 3, we exclude all these border events, since a small fraction of those photons have an incorrect energy, typically due to the registration of a double event pattern as a single event. After subtracting the expected out-of-time events from the image, we corrected the residual for vignetting and exposure using the latest calibrations (Lumb et al. 2003), which have been incorporated within the XMMSAS version 6.0 release.

Emission from A478 fills the entire *XMM-Newton* field of view, so it was not possible to determine the background level reliably from this data set. Therefore, an observation of the *Chandra* Deep Field South was used to provide an estimate of the background. We have confirmed that this choice of data set is well matched to the detector background in the 10–15 keV band for our observation of A478. However, for the goal of the current analysis the choice of the background is less important, since the measured flux is strongly dominated by emission from the cluster.

3. *CHANDRA* SPECTRAL ANALYSIS

A global spectrum of A478 was extracted from the emission filling the entire S3 chip, excluding contaminating sources. The spectrum was grouped to a minimum of 20 counts per bin to enable us to use the χ^2 fit statistic. The CCD detector responses vary as a function of position within our spectral extraction region. We therefore generated composite response files using the CIAO tasks `mkwarf` and `mkrmf` by averaging the contributions made from those parts of the detector with different responses and weighting each component according to the distribution of counts in the 0.5–2.0 keV band.

Using XSPEC version 11.3.0, a single-temperature MEKAL hot-plasma model combined with a Wisconsin absorption model (WABS) Galactic absorption component was fitted to the data between 0.7 and 7.0 keV to maximize the signal-to-noise ratio (S/N). This yielded a best-fit temperature of 6.56 ± 0.06 keV,

---

[4] See http://cxc.harvard.edu/contrib/maxim/bg.

[5] See http://asc.harvard.edu/cont-soft/software/corr_tgain.1.0.html.

[6] See http://cxc.harvard.edu/contrib/maxim/acisbg.

TABLE 1
SPECTRAL-FITTING RESULTS FOR 0.7–7.0 keV

R_{out}[a] (arcsec)	Chandra				XMM-Newton			
	kT (keV)	$Z_\odot$	n_H (10^{21} cm^{-2})	χ^2/dof	kT (keV)	$Z_\odot$	n_H (10^{21} cm^{-2})	χ^2/dof
21................	4.25 ± 0.08	0.47 ± 0.03	2.98 ± 0.06	459.8/346	4.43 ± 0.06	0.32 ± 0.01	2.87 ± 0.04	1367.8/1006
43................	6.14 ± 0.16	0.35 ± 0.03	2.86 ± 0.05	434.7/376	5.67 ± 0.07	0.28 ± 0.01	2.83 ± 0.04	1456.2/1150
61................	6.76 ± 0.20	0.36 ± 0.04	2.81 ± 0.06	415.3/357	6.19 ± 0.12	0.24 ± 0.01	2.76 ± 0.04	1312.2/1083
87................	7.47 ± 0.20	0.29 ± 0.03	2.76 ± 0.06	437.6/374	6.66 ± 0.13	0.23 ± 0.01	2.71 ± 0.04	1197.7/1095
123..............	7.67 ± 0.28	0.30 ± 0.03	2.74 ± 0.06	455.3/379	6.57 ± 0.12	0.26 ± 0.02	2.69 ± 0.04	1325.2/1096
175..............	7.91 ± 0.31	0.26 ± 0.04	2.64 ± 0.06	443.5/385	7.06 ± 0.13	0.23 ± 0.02	2.62 ± 0.04	1189.4/1116
250..............	8.12 ± 0.37	0.27 ± 0.05	2.67 ± 0.07	454.1/379	6.93 ± 0.16	0.20 ± 0.02	2.57 ± 0.05	1039.3/1058
355..............	...	...	...	...	6.96 ± 0.21	0.25 ± 0.03	2.20 ± 0.06	1025.5/1002
506..............	...	...	...	...	6.87 ± 0.35	0.32 ± 0.05	2.18 ± 0.11	1095.8/975
720..............	...	...	...	...	5.92 ± 0.57	0.38 ± 0.11	2.40 ± 0.25	1035.0/1030

[a] Outer radius of annulus. The redshift was fixed at 0.088 for all spectra. All errors are 1 σ.

with a metallicity of 0.33 ± 0.01 $Z_\odot$ and an absorbing column of $(2.91 \pm 0.01) \times 10^{21}$ cm^{-2}. The redshift was also left free to vary, giving a best-fit value of $0.0879^{+0.0003}_{-0.0012}$, which agrees well with the optical value of 0.0881 ± 0.0009 (Struble & Rood 1999). We note that S03 found the following spectral parameters on the basis of their 0.7–8.0 keV analysis of data from the S2, S3, and S4 CCDs combined using this observation: $kT = 7.18 \pm 0.11$ and $N_H = (2.59 \pm 0.03) \times 10^{21}$ cm^{-2}, with an abundance of 0.37 ± 0.02 $Z_\odot$ (all at 90% confidence). The differences are not surprising, since the gas temperature shows a marked decrease in the cluster center and the metallicity and absorbing column both exhibit central enhancements (see § 3.1) beyond the S3 chip, to which we restrict our analysis. However, the significant discrepancy in the absorbing column is mainly due to the improvement in the Chandra calibration since the Sun et al. analysis, a factor which we will return to in § 4.

3.1. Chandra versus XMM-Newton

In view of our intention to exploit the complementary properties of Chandra and XMM-Newton by combining spectral data from both (see § 4), we present here a detailed comparison of results obtained from the two observatories. We are further motivated by the apparent discrepancy between the temperatures inferred from Chandra and XMM-Newton observations of A478, as reported by Pointecouteau et al. (2004). Given the potential for spatial variation in cluster gas properties (as well as in the absorbing column), we perform a direct comparison of spectral properties in a series of contiguous annuli. Ten logarithmically spaced radial bins were defined out to a maximum radius of 12′ (see Table 1), centered on the peak of the emission as measured using Chandra (R.A. = $4^h13^m25^s.2$, decl. = $10°27′53″$). The innermost bin radius was increased to 21″ to reduce the effect of scattering between bins due to the comparatively broad point-spread function (PSF) of XMM-Newton. Equivalent Chandra spectra were extracted in the seven innermost annuli fully covered by the S3 chip.

Absorbed MEKAL models were fitted to each spectrum as before, and radial profiles of temperature, metallicity, and absorbing column are plotted in Figures 1–3, respectively, showing the Chandra data as crosses and the XMM-Newton data as diamonds. The temperature profile is typical of a "cool-core" cluster, showing a sharp drop toward the center, within ∼1′. The region outside the core is roughly isothermal, with some indication of a negative gradient farther out. It is also clear that the Chandra points are systematically higher in temperature than

those from XMM-Newton. This discrepancy persists in the measured abundances, with Chandra again giving somewhat higher values than XMM-Newton in all annuli (Fig. 2). Nonetheless, both observations show an increase in the gas metallicity in the cluster core, approximately coincident with the observed decrease in temperature in this region. Vikhlinin et al. (2005) present a recent analysis of the A478 Chandra data, which incorporates the latest calibration. Their projected temperature profile is similar to our own, although it extends beyond the S3 chip, reaching a slightly hotter peak of ∼9 keV at roughly 150″.

Furthermore, the inferred absorption column also rises toward the center, and there is close agreement between the Chandra and XMM-Newton results (Fig. 3). Also plotted is the Galactic absorption of 1.51×10^{21} cm^{-2} based on H I observations (Dickey & Lockman 1990) interpolated to the center of A478. It can be seen that the fitted points lie well above this line, implying an observed absorption roughly twice as high. However, this
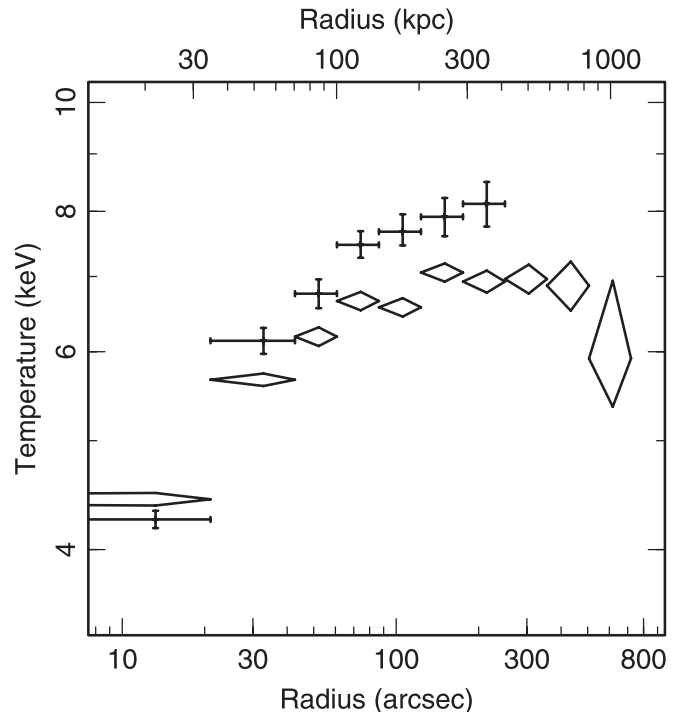

FIG. 1.—Projected gas temperature as a function of radius, showing the XMM-Newton pn data (diamonds) and the Chandra data (crosses).
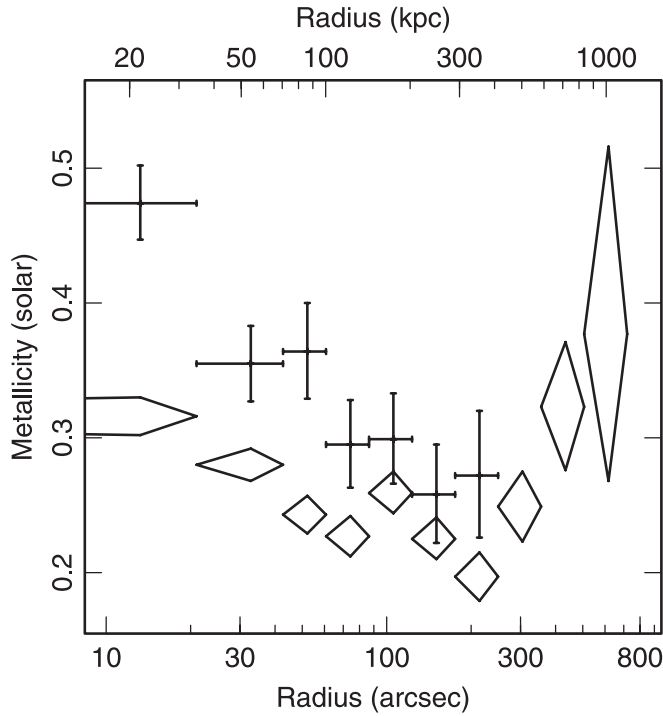
FIG. 2.—Projected gas metallicity as a function of radius, showing the *XMM-Newton* pn data (*diamonds*) and the *Chandra* data (*crosses*).

FIG. 4.—ACIS spectrum at 6.0–6.8 keV, best-fitting MEKAL model, and residuals from annuli 4–7 combined (see text for details).

excess is not localized to the cluster core and is probably associated with absorption in our galaxy (Pointecouteau et al. 2004). This behavior is not unexpected, since H I measurements become an increasingly unreliable predictor of the total Galactic absorption for columns exceeding $\sim 6 \times 10^{20}$ cm^{-2} due to contributions from molecular hydrogen, for example (Lockman 2005). An excess absorption was also inferred from photometric observations
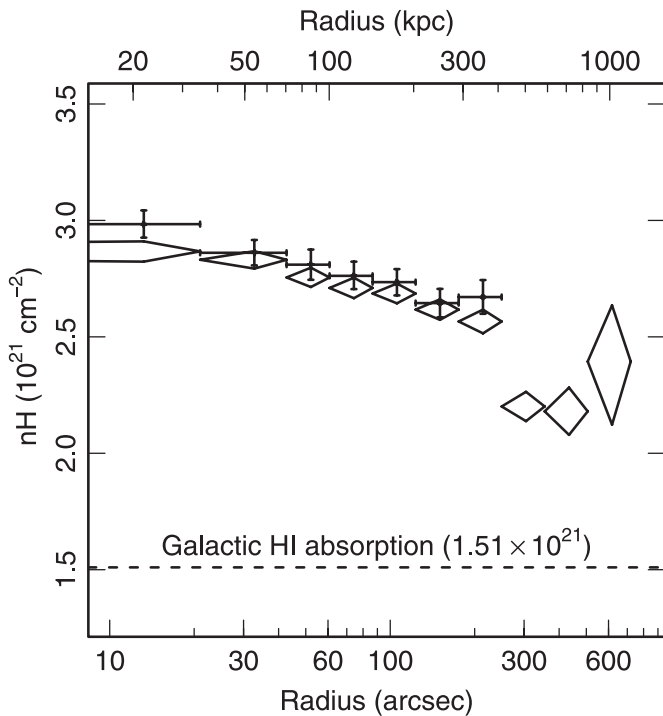

FIG. 3.—Projected absorbing column as a function of radius, showing the *XMM-Newton* pn data (*diamonds*) and the *Chandra* data (*crosses*). The H I inferred absorption value is indicated by the dotted line.
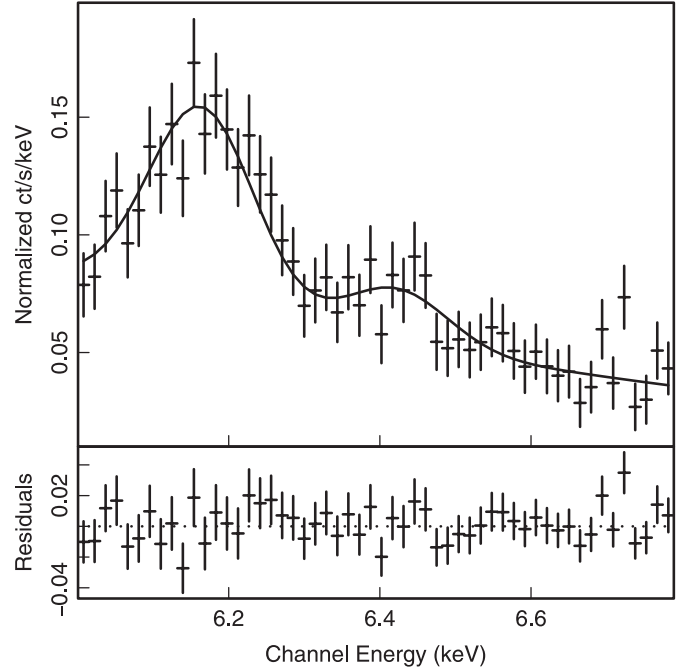
by Garilli et al. (1996), who noted that the early-type galaxies in A478 are much redder than expected.

In light of the disagreement in both temperature and metallicity between *Chandra* and *XMM-Newton*, we performed additional tests to verify the impact of any calibration errors on our results. Specifically, we checked the ionization temperature of the ICM, as measured from the prominent iron line redshifted to ~ 6.1 keV in the observer frame. We extracted a spectrum from annuli 4–7 combined, thus excluding the inner cluster core, which contains gas at a wide range of temperatures and metallicities, as already seen. This spectrum was fitted with an absorbed MEKAL model as before, in the ranges 0.7–7.0 keV and 6.0–6.8 keV (see Fig. 4). Since the absorbing column was poorly constrained when fitting the narrow (high) energy range, we fixed it at the value obtained from the 0.7–7.0 keV fit. However, we also tried fixing N_H at the Galactic value deduced from H I observations (1.51×10^{21} cm^{-2}). This made no appreciable difference to the results, which are summarized in the left half of Table 2. The corresponding χ^2 and degrees of freedom (dof) are 711.07/427 and 39.49/51 for the broad and narrow range *Chandra* fits, respectively. It is clear from the broadband fit that, even within this apparently roughly isothermal region, the cluster emission is not well described by a single-temperature plasma. This hints at significant spatial variation in the temperature of the ICM, a possibility that we investigate further in § 5.3.

For direct comparison, the equivalent test was performed on the *XMM-Newton* pn spectrum from annuli 4–7; the results are summarized in the right-hand side of Table 2. As with *Chandra*, it was necessary to fix N_H for the narrowband fit at the optimum value obtained from the 0.7–7.0 keV fit. Once again, we checked that the results do not change noticeably when N_H was fixed at the H I value. However, we did find that freezing the redshift at the optical value of 0.088 produced an unacceptable fit (χ^2/dof = 423.20/154), indicative of a small calibration offset, also found by Pointecouteau et al. (2004) and de Plaa et al. (2004). This is due to the uncertainty in the current charge transfer inefficiency correction affecting the pn detector in extended full-frame mode

TABLE 2
Spectral-Fitting Results for Annuli 4−7 Combined

| Fit Range (keV) | Chandra | | | | XMM-Newton | | | |
	kT (keV)	$Z_\odot$	n_H (10^{21} cm^{-2})	χ^2/dof	kT (keV)	$Z_\odot$	n_H (10^{21} cm^{-2})	χ^2/dof
0.7–7.0	7.73 ± 0.15	0.28 ± 0.02	2.72 ± 0.03	711.1/427	6.81 ± 0.06	0.28 ± 0.01	2.66 ± 0.02	1338.0/1256
6.0–6.8	6.49 ± 0.61	0.22 ± 0.05	2.72 (frozen)	39.5/51	6.69 ± 0.26	0.24 ± 0.02	2.66 (frozen)	158.5/152

Notes.—The redshift was fixed at 0.088 for *Chandra* but was left free to vary for the *XMM-Newton* broadband fit; a simple linear gain offset was fitted to the narrowband *XMM-Newton* spectrum to give the correct redshift (see text for details). All errors are 1 σ.

only (K. Dennerl 2004, private communication), a correction which has only just been incorporated into the XMMSAS 6.1 release. Leaving the redshift free to vary produced a best-fit value of 0.074 ± 0.001. To provide a fairer comparison with *Chandra* in a region heavily dominated by emission line flux, we therefore applied a small modification to the response matrix file to improve the fit, using the XSPEC command `gain`. This produced an acceptable fit with a χ^2/dof of 158.65/154, compared to 1337.99/1261 for the broad-range fit, without the gain modification. The two fitted gain parameters were frozen at their best-fit values in the calculation of MEKAL parameter errors.

Table 2 shows that the broadband *Chandra* spectrum produces an anomalously high temperature, which disagrees with the *Chandra* ionization temperature measurement, as well as with both the broadband and ionization temperature fits from *XMM-Newton*. This could indicate a problem with the ACIS calibration as the source of the discrepancy between *Chandra* and *XMM-Newton* reported by Pointecouteau et al. (2004) and seen in Table 2 for this data set. However, this behavior can be explained by significant temperature variation within each annulus, giving rise to different characteristic average temperatures when folded through the *Chandra* and *XMM-Newton* responses and fit with a single-phase plasma model (see § 5.3). The implication is that better agreement between *Chandra* and *XMM-Newton* ought to occur for spectra extracted from approximately isothermal regions, which we find to be the case (see § 5.3).

In the meantime, we have neglected to correct for this bias in what follows, in view of the impracticality of restricting our *Chandra* analysis to a small high energy range and given the somewhat better agreement between *Chandra* and *XMM-Newton* seen in the deprojected temperature profile (see § 4).

3.2. *The Effects of Multiphase Gas*

In order to shed some light on the discrepancy between the *Chandra* and *XMM-Newton* results described above, we have

conducted a series of simulations of multiphase spectra, which we have fitted with a single-temperature spectrum. We have used the spectral responses and background spectrum from annuli 4−7 (see Table 2) for both telescopes and assumed a value of Galactic absorption of 2.7×10^{21} cm^{-2} for all these simulations. Initially, we generated 1000 realizations of a spectrum comprising four temperature components (6, 6.5, 7.5, and 8 keV, weighted in the ratio $7:10:30:7$), with an abundance of 0.3 $Z_\odot$. The results of fitting this spectrum with a single absorbed MEKAL model recovered the following mean temperatures and standard deviations: 7.11 ± 0.10 (*Chandra*, 0.7–7.0 keV), 7.12 ± 0.06 (*XMM-Newton*, 0.7–7.0 keV), 7.16 ± 0.45 (*Chandra*, 6.0–6.8 keV), and 7.17 ± 0.19 (*XMM-Newton*, 6.0–6.8 keV). The excellent agreement between these four cases demonstrates that moderately multiphase gas with the same metallicity cannot account for the discrepancies seen in Table 2, despite the differences in the spectral responses for *Chandra* and *XMM-Newton*.

We then simulated a spectrum with two temperature components (5 and 12 keV) and an abundance of 0.3 $Z_\odot$ (case A), 0.2 and 0.5 $Z_\odot$ (case B), and 0.5 and 0.2 $Z_\odot$ (case C). The fitting results are summarized in Table 3. It can be seen that there is consistently good agreement between *Chandra* and *XMM-Newton* in all three cases. Furthermore, it can also be seen that the 0.7–7.0 and 6.0–6.8 results are generally in good agreement when both have the same metallicity. However, when the hotter phase has higher metallicity, the narrowband ionization balance fit yields a significantly hotter temperature for both *Chandra* and *XMM-Newton*. Conversely, when the cooler phase is more enriched, the 6.0–6.8 keV fit yields a cooler temperature, albeit at rather lower significance.

As an aside we note that, in all cases, the metallicity obtained with a single-temperature fit to the multiphase spectra overestimates the input values, by ∼25% in the simple case in which the two phases have the same abundance. Whenever the metallicities of the two phases differ, the abundance is overestimated by an even greater amount, for both the broad- and narrowband fits.

TABLE 3
Spectral-Fitting Results for Simulated Multiphase Spectra

| Simulation | Chandra | | | | | XMM-Newton | | | |
	Fit Range (keV)	kT (keV)	$Z_\odot$	n_H (10^{21} cm^{-2})	χ^2/dof	kT (keV)	$Z_\odot$	n_H (10^{21} cm^{-2})	χ^2/dof
A	0.7–7.0	7.28 ± 0.12	0.37 ± 0.02	2.66 ± 0.03	439.1/427	7.36 ± 0.06	0.38 ± 0.01	2.65 ± 0.02	1294.6/1260
A	6.0–6.8	7.65 ± 0.63	0.39 ± 0.08	2.70 (frozen)	51.8/51	7.70 ± 0.28	0.39 ± 0.04	2.70 (frozen)	157.7/155
B	0.7–7.0	7.50 ± 0.15	0.38 ± 0.03	2.65 ± 0.04	443.4/427	7.67 ± 0.09	0.39 ± 0.01	2.61 ± 0.02	1324.4/1260
B	6.0–6.8	9.19 ± 0.57	0.54 ± 0.10	2.70 (frozen)	51.5/51	9.16 ± 0.22	0.53 ± 0.04	2.70 (frozen)	156.9/155
C	0.7–7.0	7.03 ± 0.11	0.49 ± 0.03	2.67 ± 0.03	455.7/427	7.07 ± 0.06	0.48 ± 0.01	2.67 ± 0.02	1331.4/1260
C	6.0–6.8	6.45 ± 0.53	0.41 ± 0.08	2.70 (frozen)	51.5/51	6.46 ± 0.24	0.39 ± 0.04	2.70 (frozen)	157.6/155

Notes.—Input spectra comprise equally weighted 5 and 12 keV components with equal abundance of 0.3 $Z_\odot$ (A), 0.2 and 0.5 $Z_\odot$ (B) and vice versa (C), respectively. Errors are the standard deviation of the 1000 Monte Carlo realizations in each case.

On the basis of these simulations, we therefore conclude that the discrepancy we observe between the *Chandra* results and the *XMM-Newton* results cannot readily be explained by the presence of multiple temperature components, even with differing abundances.

4. DEPROJECTION ANALYSIS

To determine the intracluster gas properties, we implemented a standard "onion peeling" scheme to deproject the X-ray data, under the assumption of spherical symmetry. The spectral deprojection was performed using the PROJCT model in XSPEC, using a single-temperature MEKAL plasma model with a Galactic absorption component (WABS). Only data in the range 0.7–7.0 keV were used, and each spectrum was grouped to a minimum of 20 counts per bin, including the background contribution. The foreground absorbing column density was left free to vary in each annulus, as was the MEKAL temperature, abundance, and normalization.

The XSPEC MEKAL normalization is defined as

$$K = \frac{10^{-14}}{4\pi[D_A(1+z)]^2} \int n_e n_H \, dV, \qquad (1)$$

where D_A is the angular diameter distance, z is the redshift, and dV is the volume from which the deprojected emission originates. The best-fit normalization for each spectrum was converted directly into a mean gas density in the corresponding spherical shell, assuming a number density ratio given by

$$n_e = \frac{\mu_H}{\mu_e} n_H = 1.20 n_H, \qquad (2)$$

appropriate for a fully ionized plasma with a metallicity of 0.3 times the solar value, using our adopted abundance table from Anders & Grevesse (1989).
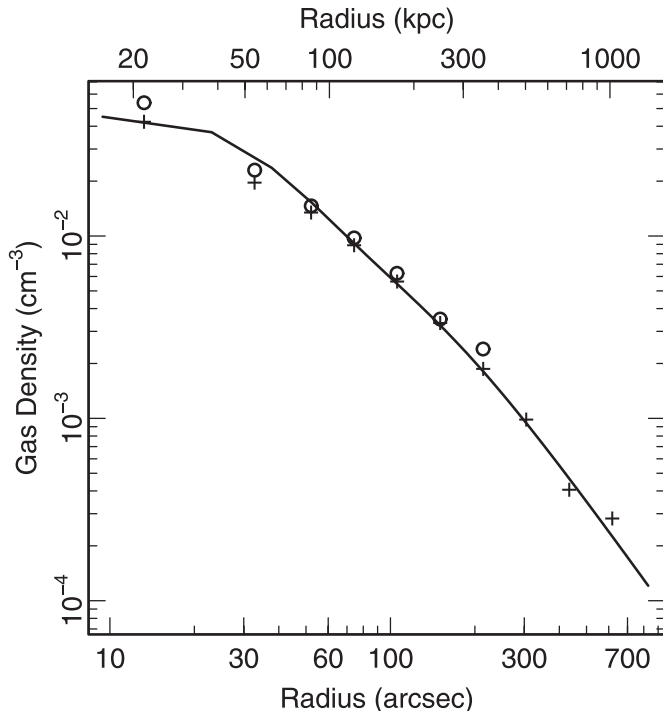
Fig. 5.—Gas electron number density as a function of radius, showing the *Chandra* points (*circles*) and *XMM-Newton* data (*plus signs*). Errors on the density are too small to be plotted, and the radial bin width error bars have been omitted for clarity. Also shown is the *ROSAT* density profile from Mohr et al. (1999), plotted as a solid line for clarity.
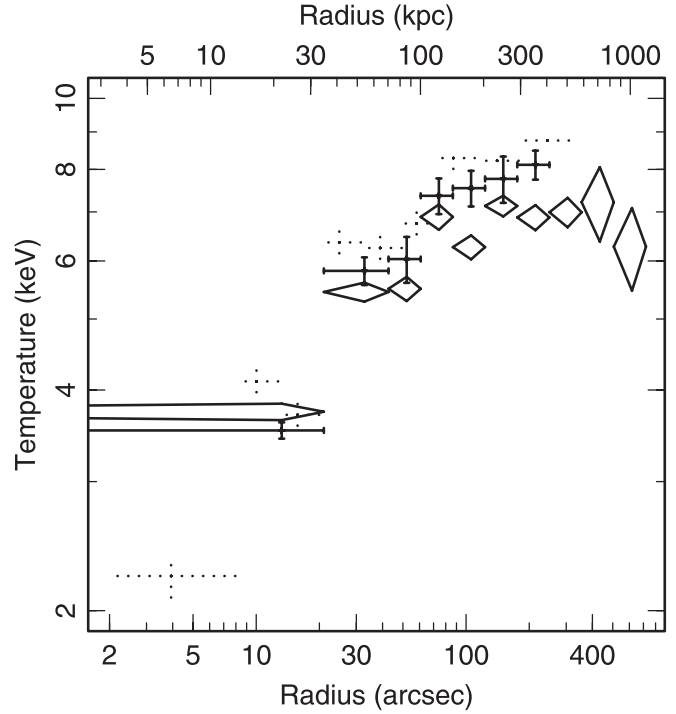
Fig. 6.—Deprojected temperature as a function of radius, showing the *XMM-Newton* pn data (*diamonds*), the *Chandra* data (*solid crosses*), and the S03 analysis of the same *Chandra* observation, using older calibration data (*dotted crosses*). Although some discrepancy between *Chandra* and *XMM-Newton* remains, it has been reduced with improvements to the CALDB and is less pronounced than in the projected $T(r)$ (Fig. 1).

Data from the outermost bin were discarded, since this volume incorporates a contribution from emission beyond the last shell that implies a nontrivial geometry for the determining the mean gas density. This leaves a total of six *Chandra* and nine *XMM-Newton* radial bins, spanning the innermost 8.′4 (835 kpc) of the ICM. Following Lewis et al. (2003), we assign an effective radius to each annulus, which is approximately equivalent to an emission-weighted mean, given by (see McLaughlin 1999)

$$r = \left[0.5\left(r_{out}^{3/2} + r_{in}^{3/2}\right)\right]^{2/3}. \qquad (3)$$

The resulting density profile is plotted in Figure 5 and also includes the data from the *Röntgensatellit* (*ROSAT*) analysis of Mohr et al. (1999), shown as the solid line. There is generally good agreement between the three sets of data, although the *Chandra* points appear to be systematically higher than those of *XMM-Newton*. It is particularly encouraging to note the close agreement between the *Chandra*/*XMM-Newton* values and the *ROSAT* profile, since the latter was derived from an analytical (double β-model with PSF corrections) fit, as compared to the nonparametric onion-peeling method used in this analysis.

The corresponding deprojected gas temperature profile is shown in Figure 6, with the *Chandra* and *XMM-Newton* points plotted as before. It can be seen that the *Chandra* temperatures are hotter, except for the innermost bin, where PSF scattering acts to smooth out the gradient in the *XMM-Newton* data. However, the agreement between the two observations is better than in the projected $kT(r)$, with an overlap in the 1 σ error bounds for all but three annuli. The deprojected temperature gradient is steeper than that observed in the projected profile (Fig. 1), as expected (since projection smooths out any such gradients), and reaches a minimum central value of ~3.5 keV. Also shown, for comparison,

are the points from S03 using the same *Chandra* data, plotted as dotted crosses. These temperature values are systematically hotter than our measurements. We attribute this discrepancy to changes in the *Chandra* calibration between CALDB version 2.15 and CALDB version 2.26, particularly with respect to the method for handling the effects of the ACIS contamination, which causes an energy-dependent absorption that can affect temperature estimates. As can be seen, the newer ACIS calibration produces temperatures that are more consistent with those from *XMM-Newton*.

5. SPECTRAL-MAPPING ANALYSIS

5.1. *Hardness Method*

Although the surface brightness of A478 appears to exhibit a smooth morphology typical of a relaxed cluster, it is difficult to gauge the true state of the gas from studying the images alone. Here we describe the process of creating a temperature map from the *Chandra* X-ray data, which is based on a wavelet-smoothed hardness ratio image (Finoguenov et al. 2004b). The key advantage of this approach is that it allows fine-scale temperature structure to be resolved without any prior knowledge of its morphology, since we are able to work with high-resolution images of the cluster.

We select two hardness bands, with the following energy ranges: 0.5–2.0 keV (soft band) and 2.0–7.0 keV (hard band). The hardness ratio (given by the hard-band flux divided by the soft-band flux) depends strongly on the gas temperature and the absorbing column along the line of sight, as well as more weakly on the metallicity of the gas. Under the assumption that the variation in absorbing column over the S3 chip is small (see the crosses in Fig. 3), we can therefore use the hardness ratio to estimate the temperature directly.

Taking the best-fit model to the global spectrum (§ 3), we fix the abundance and absorbing column and generate a series of 200 new models with different temperatures in the range 0.5–15.0 keV. For each of these spectra, we evaluate the ratio of the predicted model flux in the hard to soft bands. We then fit a sixth-order polynomial curve to the data to obtain an expression for the gas temperature as a function of hardness. The residuals from this best-fit relation are less than 1% throughout the range of hardness values to which we apply it.

To create a hardness ratio map from X-ray data it is necessary to apply some smoothing to suppress Poisson fluctuations. This ensures nonzero pixel values in the denominator (soft-band image) but can also reveal subtle variations in hardness on small scales. We use a wavelet decomposition approach, which is ideal for highlighting low surface brightness diffuse emission, even in the presence of bright embedded point sources while retaining complex structural information (see Vikhlinin et al. [1998] for details). This approach also provides information on the significance of structures identified on each scale and has recently been used in the analysis of *XMM-Newton* observations of several clusters (Finoguenov et al. 2004a, 2004b; Henry et al. 2004).

Initially, we extract source and background images and corresponding exposure maps in both the soft and the hard bands for the whole S3 chip. The corresponding background image is then subtracted from each hardness image, and the resulting image is divided by the appropriate exposure map. The exposure maps are obtained by weighting the contributions to the effective area of the detector by the best-fitting model to the global spectrum fitted in § 3, within each of the soft and the hard bands separately. Pixels with an equivalent exposure less than 25% of the highest value within the S3 chip were masked out to improve the S/N of the resulting hardness image.

A wavelet transform decomposition was then applied separately to the soft- and hard-band images over six different scale sizes, increasing in integer powers of 2 from 2^2 to 2^7 pixels, corresponding to angular sizes of $\sim 2''$ and $\sim 1'$, respectively. A 5 σ threshold was used to identify genuine sources, whose extent was defined to enclose those neighboring pixels lying above a 2 σ threshold. Following Finoguenov et al. (2004b), an additional smoothing was applied to each wavelet transform in turn, by convolving it with a Gaussian kernel of width equal to that scale, to reduce discontinuity artifacts associated with separating the image into different scales. The soft- and hard-band images were reconstructed by summing all six smoothed wavelet–transformed images obtained at each of the scale sizes. The final hardness map was obtained as the ratio of the hard to soft images. Each pixel was then converted into a temperature value by using the polynomial relation derived above, with unphysical hardness values (confined to a few pixels near the S3 chip boundary) masked out of the resulting temperature map (i.e., values lying outside the fitting range of the calibration curve).

5.2. *Spectral-Fitting Method*

There are several key assumptions of the hardness-based approach to generating a temperature map that could produce incorrect results. Specifically, there may be subtle, small-scale variations in absorbing column and gas metallicity that could manifest themselves as spurious features in the inferred temperature distribution. Here we present a more sophisticated method to determine spatial variations in gas temperature in order to assess the validity of the above technique.

With an estimated temperature map we are well positioned to identify interesting features in the image for targeting with a conventional spectral-fitting approach. Using contour maps of the temperature and soft-band images, we defined a series of 53 separate regions, each containing a minimum of 1000 counts in the raw image, originating from gas of similar projected temperature and surface brightness, as implied by our wavelet decomposition analysis.

We extract source and background spectra and response files in each of these 53 regions and fit each with an absorbed MEKAL model as before. Images of these regions, showing the best-fit temperature and 1 σ bounds, are plotted in the lower half of Figure 7. The color table for the spectral fit temperature map is identical to that used in the hardness temperature maps in the upper half of the figure. The broad features in the hardness map are confirmed in the spectral map: specifically, the temperatures of the cool core and surrounding regions agree very well. Moreover, the spectral analysis confirms the existence of four prominent hot spots located around the cluster center, with temperatures as high as 12 keV, almost double that of the surrounding medium in all cases, albeit with large uncertainties. The origin of these hot spots is unclear, but it seems unlikely that they can all be attributed to point-source contamination: visual inspection of the raw image reveals no evidence for a surface brightness excess at these locations. We return to the interpretation of these features in § 6.1.

5.3. *Spectral-Mapping Deprojection*

Using our spectral-mapping results, it is possible to perform an approximate deprojection to provide a comparison with the onion-peeling method. To achieve this, we assume that all the emission projected onto each region originates in a spherical shell bounded by the inner- and outermost radii enclosing the region, measured from the surface brightness centroid used previously. The volume used to calculate the gas density from the MEKAL
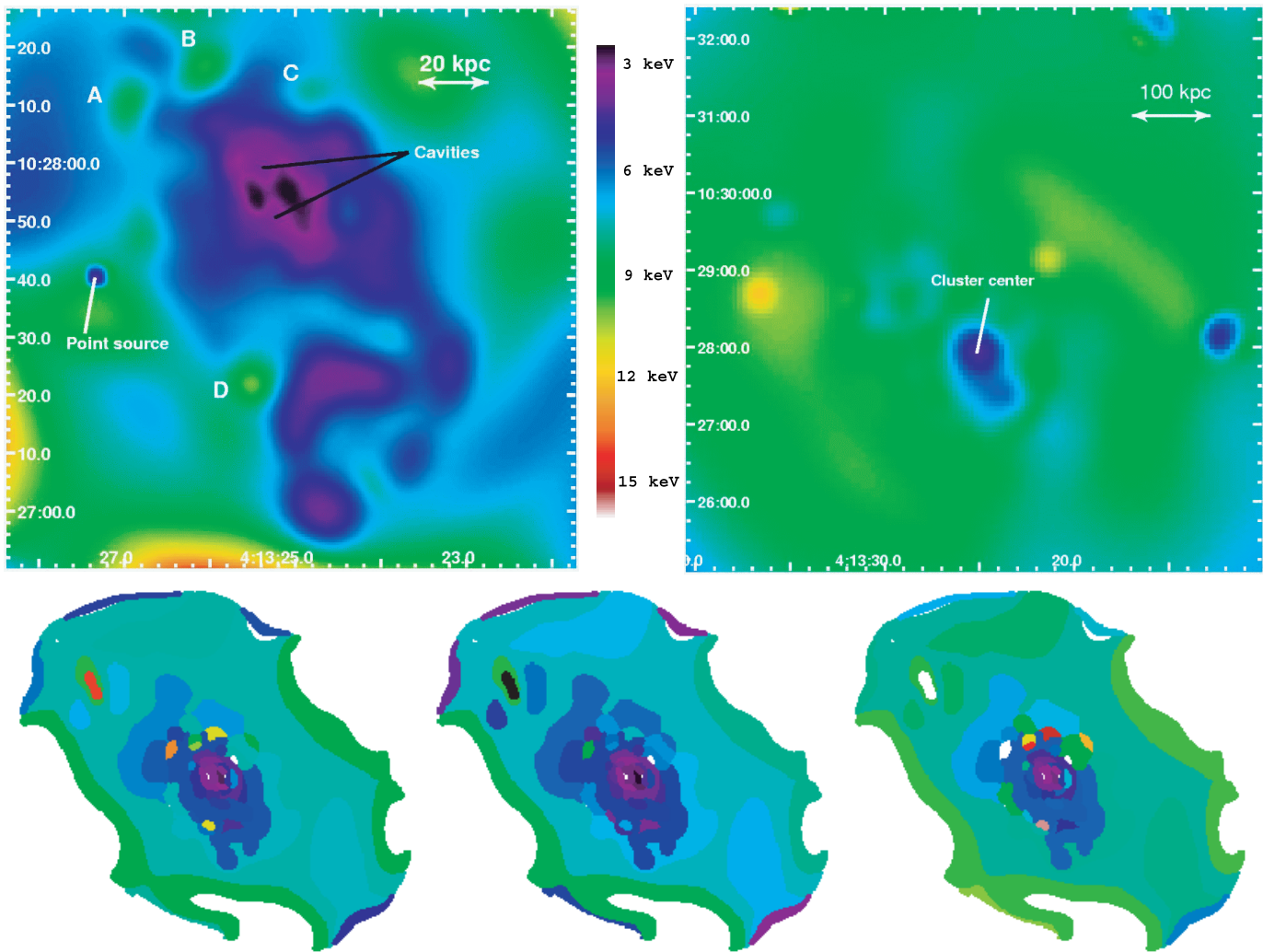
Fig. 7.—Wavelet-smoothed temperature maps of A478 from *Chandra* (*top left*) and *XMM-Newton* (*top right*), derived from the hardness ratio method. The positions of four hot spot regions are indicated by the letters A–D, and the cavities discovered by S03 are also labeled. *Bottom*: *Chandra* temperature map derived from the spectral-fitting method. *Left to right*, best-fit values, 1 σ low and upper limits on the temperature. The innermost green, yellow, and orange regions are the hot spots.

normalization (eq. [1]) is formed from the intersection of this shell with the cylinder having the cross section of that region. A more detailed description of this approach is presented in Henry et al. (2004).

In this "deprojection" scheme, no attempt is made to model out or otherwise remove the contaminating emission from regions outside the volume element under consideration, which are projected onto the spectral region. Therefore, we take the projected temperature and metallicity information to apply to the three-dimensional volume element. However, in selecting these regions we have ensured that that gas is essentially isothermal as measured in projection, which minimizes the additional smoothing effect of averaging over a range of temperatures. Correspondingly, the inferred temperatures and abundances are more likely to be representative of the deprojected gas properties.

A plot of the temperature profile from the mapping analysis is presented in Figure 8, with the radial axis expressed in units of R_{500} (1349 kpc), as determined from our mass model of the cluster (see § 5.4). It can be seen that there is a large degree of temperature scatter, with the hot spots clearly visible, albeit with large errors. The overlap between the *Chandra* and *XMM-Newton* spectral-mapping data is somewhat limited, due to the poorer spatial resolution of *XMM-Newton* combined with the impact of

edge effects in the wavelet reconstruction limiting the outer radius of data from the *Chandra* S3 chip. However, it can be seen that the discrepancy between the *Chandra* and the *XMM-Newton* results found in the annular spectral fits is not apparent in the spectral-mapping data. Although this is due in part to the larger uncertainties in the data points, it may also point to the source of the discrepancy being the varied temperature structure in the ICM, which gives rise to a range of temperatures within a given annulus. Since *XMM-Newton* is more sensitive to cooler temperatures and *Chandra* is more sensitive to hotter ones, such a situation is likely to lead to a bias in fitting a single-temperature spectrum, as observed. Moreover, the iron ionization fit is more sensitive to cooler gas phases, which emit proportionately more line flux, which explains why the *Chandra* 6.0–6.8 keV result (Table 2) was in good agreement with that of *XMM-Newton*.

Figure 9 shows the entropy profile from the spectral-mapping analysis. Also shown, as a dashed line, is a fit of the form $S \propto r^{1.1}$ (cf. Tozzi et al. 2000), which has been shown to provide a good match to the outer regions of most reasonably relaxed clusters (Ponman et al. 2003). To highlight the trend in the data, the points have been smoothed using a locally weighted regression in log-log space (*solid line*). This technique smooths the data using a quadratic function that is moved along the set of points to build
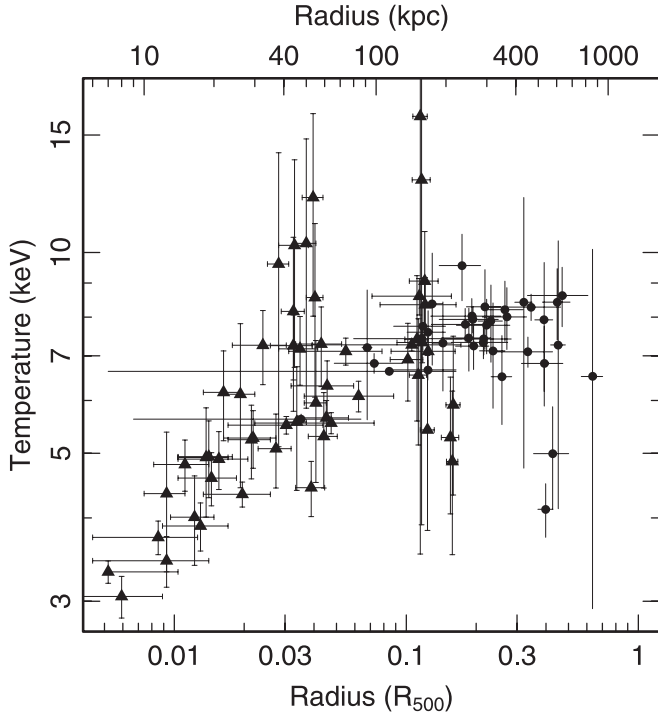
Fig. 8.—Temperature profile from the spectral-mapping analysis. No discrepancy between the *Chandra* (*diamonds*) and *XMM-Newton* (*circles*) points is evident in the mapping data.
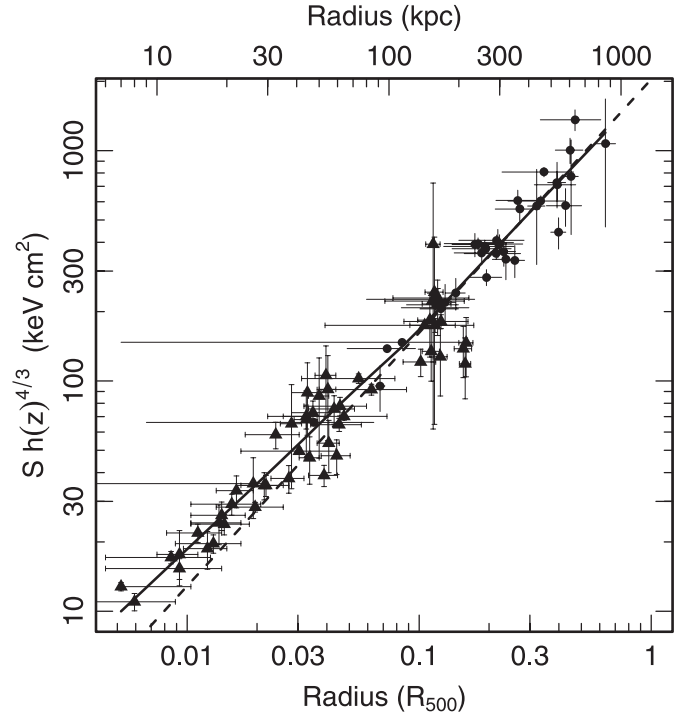
Fig. 9.—Entropy profile from the spectral-mapping deprojection. The symbols are the same as in Fig. 8. The dashed line is an unweighted fit to the data, of the form $S \propto R^{1.1}$. For comparison, the solid line shows a locally weighted regression of the data in log-log space, using the method described in § 6.1.

up a curve, in an analogous fashion to how a moving average is computed for a time series. The algorithm used is implemented in the LOWESS function in the R Project statistical environment package[7] (ver. 2.0.0, R Development Core Team 2005), and further details can be found there. The agreement in the outer regions between this curve and the $S \propto r^{1.1}$ line is striking, although the data deviate slightly above this simple relation in the cool core (within $\sim 0.1 R_{500}$; see Fig. 8). We defer further discussion of this issue to § 6.3.

5.4. *Mass Distribution*

The deprojected gas $T(r)$ and $\rho(r)$ can be used to infer the gravitating mass profile, assuming hydrostatic equilibrium, given by

$$M_{grav}(r) = -\frac{kT(r)r}{G\mu m_p}\left(\frac{d\ln\rho}{d\ln r} + \frac{d\ln T}{d\ln r}\right) \qquad (4)$$

(e.g., Fabricant et al. 1980), where μ is the mean molecular weight of the gas and m_p is the proton mass. In order to evaluate analytically the gradients in this equation, we fit a third-order polynomial to both the $T(r)$ and $\rho(r)$ data in log space. The resulting mass profile is evaluated at the radii of the input $T(r)$ and $\rho(r)$ values and is well described by a profile of the form (e.g., Zhao 1996)

$$\rho(r) = \frac{\rho_0}{x^n(1+x)^{3-n}}, \qquad (5)$$

where ρ_0 is the central density, $x = r/r_s$, and r_s is a characteristic scale radius. For $r \ll r_s$, the profile is characterized by a cusp,

with $\rho \propto r^{-n}$. Equation (5) is the generalized form of the so-called NFW profile (Navarro et al. 1995), which is obtained for $n = 1$. A reasonable proxy for the virial radius of the halo can be obtained from r_{200}, the radius enclosing a mean overdensity of 200 with respect to the critical density, $\rho_{crit}(z)$, of the universe at the observed cluster redshift, z, given by

$$\rho_{crit}(z) = E(z)^2 \frac{3H_0^2}{8\pi G},$$

where G is the gravitational constant, H_0 is the Hubble constant at $z = 0$, and

$$E(z) = (1+z)\sqrt{1 + z\Omega_m + \frac{\Omega_\Lambda}{(1+z)^2} - \Omega_\Lambda},$$

equal to 1.042 for our adopted redshift and cosmology. The concentration of the NFW halo, c, is then obtained as r_{200}/r_s.

To provide better constraints on the mass distribution in the core of A478, we perform a finer binned onion-peeling analysis using just the *Chandra* data, which has much higher spatial resolution than *XMM-Newton* data. The resulting gas density and temperature profiles are plotted in Figures 10 and 11, together with the best-fit third-order polynomial curve (in log-log space) to the data. These smoothed curves were used to evaluate the logarithmic gradients needed to determine the mass profile using equation (4). Since we have fitted these polynomials in log-log space, the logarithmic gradient is simply the derivative of the function.

The cumulative mass distribution was calculated at the radius of the input $T(r)$ and $\rho(r)$ data but using the values of the best-fit curve rather than the measured data points. We have excluded the innermost bin since the gradient at this point is rather uncertain; we are more confident about the outermost bin since the turnover
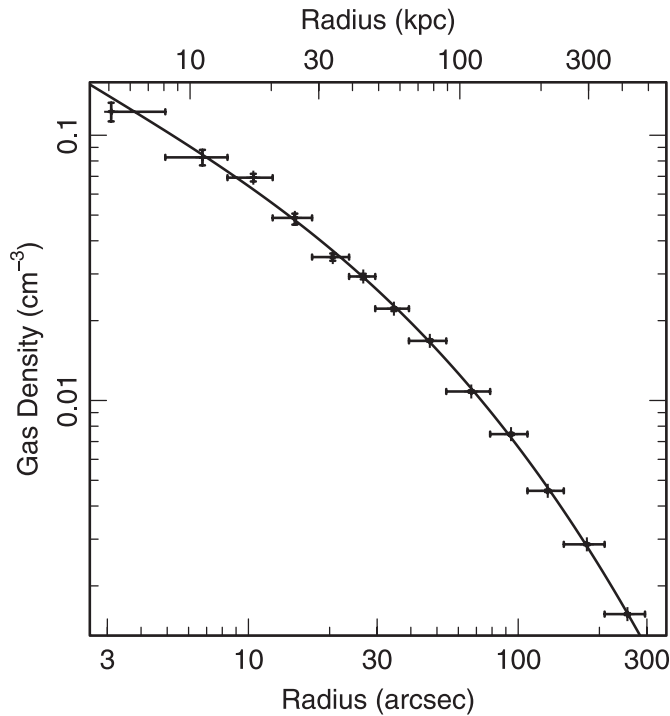
FIG. 10.—High-resolution *Chandra* gas density profile, showing the best-fit third-order polynomial relation in log-log space (*solid line*).

FIG. 12.—Mass profile from the *Chandra* data. The solid line is the best fit using eq. (5), with an inner logarithmic slope of -0.35 ± 0.22; for comparison, the dotted line shows the best-fit NFW profile (inner logarithmic slope of -1). The 1 σ errors were generated from a set of 2000 Monte Carlo simulations.

implied by the best-fit curve is consistent with the temperature profile from *XMM-Newton*, which extends beyond this radius (see Fig. 6; *diamonds*), and is also confirmed by the *Chandra* analysis of Vikhlinin et al. (2005), which extends beyond the S3 chip. The mass profile is plotted in Figure 12, together with the best-fit mass function obtained with equation (5). The errors were determined from a series of 2000 Monte Carlo realizations
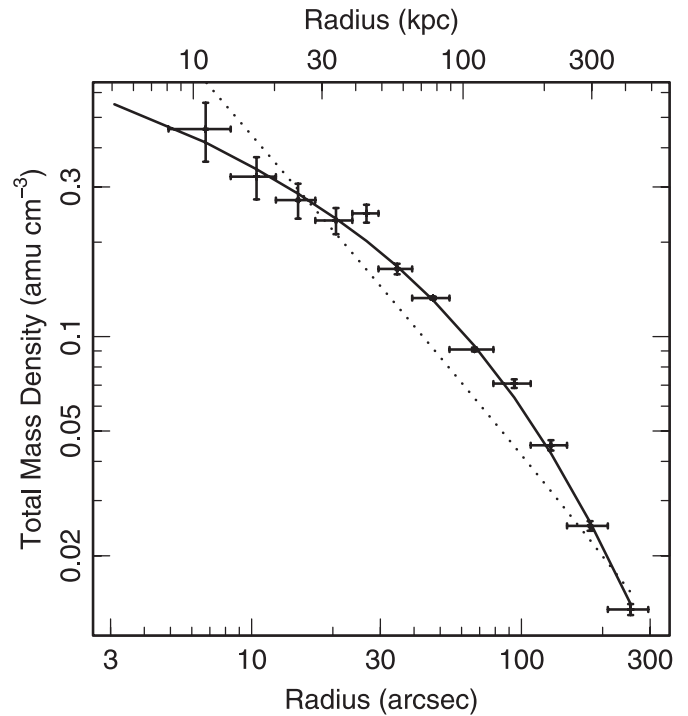
of the input $T(r)$ and $\rho(r)$ data; in each case a best-fit mass model (eq. [5]) was fitted, and the errors on the model parameters were obtained from the standard deviation of the set of points. Also plotted is the gas fraction profile (Fig. 13), which actually *decreases* with radius out to ∼200 kpc, beyond the confines of the
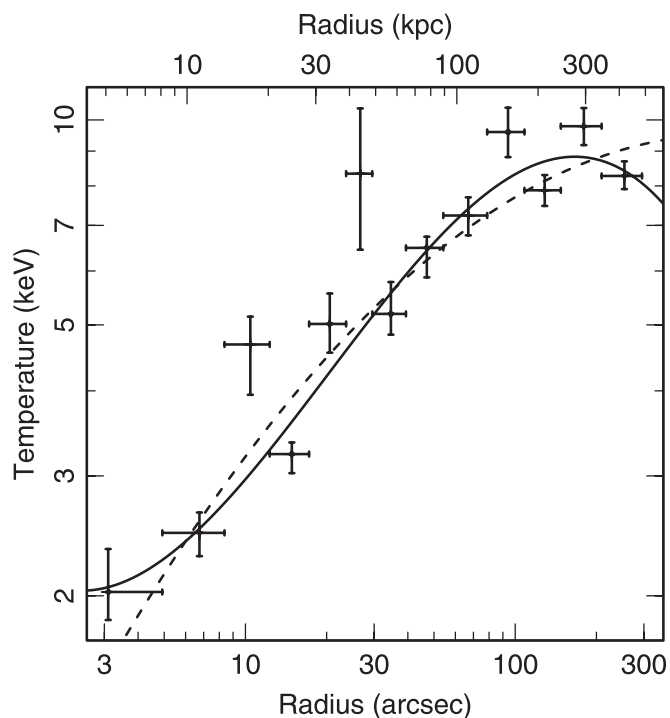

FIG. 11.—High-resolution *Chandra* gas temperature profile, showing the best-fit second-order (*dashed line*) and third-order (*solid line*) polynomial relations in log-log space, respectively.
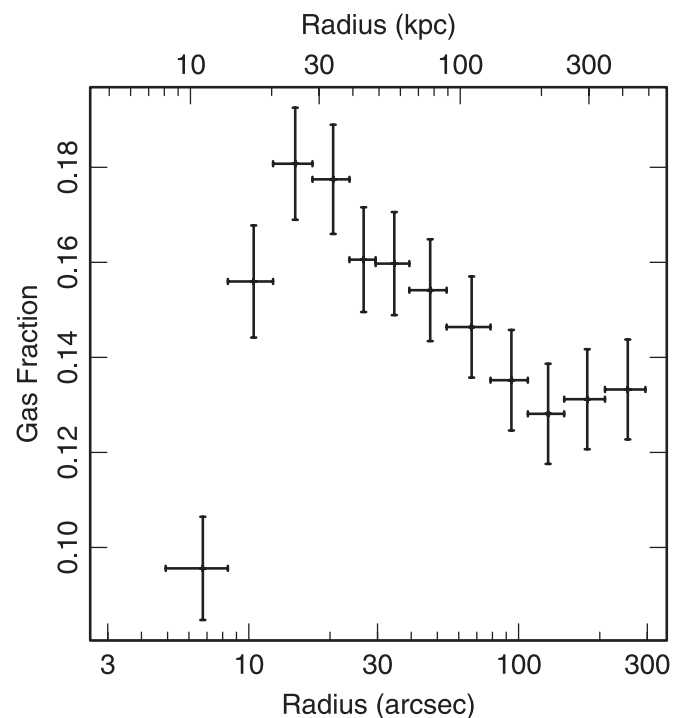

FIG. 13.— *Chandra* gas fraction profile, which shows an unusual decrease with radius within the cool core, beyond the central galaxy. The 1 σ errors were generated from a set of 2000 Monte Carlo simulations.

central galaxy, somewhat contrary to expectation (e.g., David et al. 1995; Sanderson et al. 2003).

We find a best-fit index parameter of $n = 0.35 \pm 0.22$, with a corresponding scale radius and concentration parameter of $r_s = 317 \pm 82$ kpc and $c = 6.9 \pm 1.6$, giving the values $R_{200} = 2190 \pm 125$ kpc and $R_{2500} = 620 \pm 70$ kpc. Allen et al. (2003) and Schmidt et al. (2004) also measured the *Chandra* mass profile for A478 but fitted it with an NFW profile (i.e., n fixed at 1), to give $R_{200} = 2464^{+190}_{-120}$ kpc (converted to $H_0 = 70$) and $R_{200} = 2367$ kpc, respectively. Pointecouteau et al. (2004) also fitted an NFW profile to the poorer resolution *XMM-Newton* data to derive a value of $R_{200} = 2100 \pm 100$ kpc, in reasonable agreement with our findings. We estimate a total mass within R_{200} of $(1.3 \pm 0.27) \times 10^{15}\ M_\odot$, compared to $1.84^{+0.48}_{-0.24}\ M_\odot$ for Allen et al. and $1.1 \times 10^{15}\ M_\odot$ for Pointecouteau et al.

To investigate the robustness of our $M(r)$ inner logarithmic slope measurement, we have also computed the mass profile for the case in which a second-order polynomial is fitted to the temperature points (Fig. 11; *dashed line*). In this case we recover a slightly steeper index of $n = 0.49 \pm 0.24$. However, we note that a second-order polynomial indicates a rising $T(r)$ beyond the data points, whereas the third-order polynomial curve exhibits a turnover that is clearly preferred by our *XMM-Newton* data, as well as the *Chandra* ACIS-I projected temperature profile of Vikhlinin et al. (2005). We return to discuss the mass distribution in § 6.4.

6. DISCUSSION

6.1. *Hot Spots in the ICM*

While there is generally a surprising amount of temperature structure present in the ICM in A478, of particular note are four hot spots seen in the inner regions of the core (see Fig. 7). Three of them are located to the north of the core; the other is to the south, and they all lie within ∼30–60 kpc of the center. There are no known cluster galaxies located at the position of these features, and they all lie just outside the edge of the central cluster galaxy, PGC 014685: its d_{25} diameter (the isophote at which the optical *B*-band surface brightness reaches 25 mag arcsec^{-2}) is 57 kpc (Paturel et al. 1997).

All four regions are clear outliers in both the temperature (Fig. 8) and pressure (Fig. 14) profiles but occupy a relatively small volume. Correspondingly, they produce an essentially negligible distortion in the X-ray surface brightness distribution of the core of A478. The entropy of the hot spots also appears to be systematically higher than expected. Compared to the smoothed regression relation plotted in Figure 9, an excess entropy between 20 and 50 keV cm^2 is present in each of the hot spots, corresponding to 30%–50% of the expected value. The combination of excess pressure and entropy indicates that these are strong shocks and are therefore unlikely to be the result of sound waves or mildly supersonic motion. However, the volume enclosing the hot spots is too small for them to produce a noticeable surface brightness contrast compared to the bright emission from the cool core.

Some key properties of these hot spots are summarized in Table 4, including the estimated excess thermal energy present in each one, based on the excess gas pressure and estimated volume. This excess was measured relative to an estimate of the underlying $P(r)$, obtained from a locally weighted regression of the data in log-log space (Fig. 14, *solid curve*), using the method described in § 5.3. The excess energy in each hot spot was calculated by multiplying its residual excess pressure above this curve by the estimated volume for the region. Although the errors on the individual estimates are quite large, the total excess
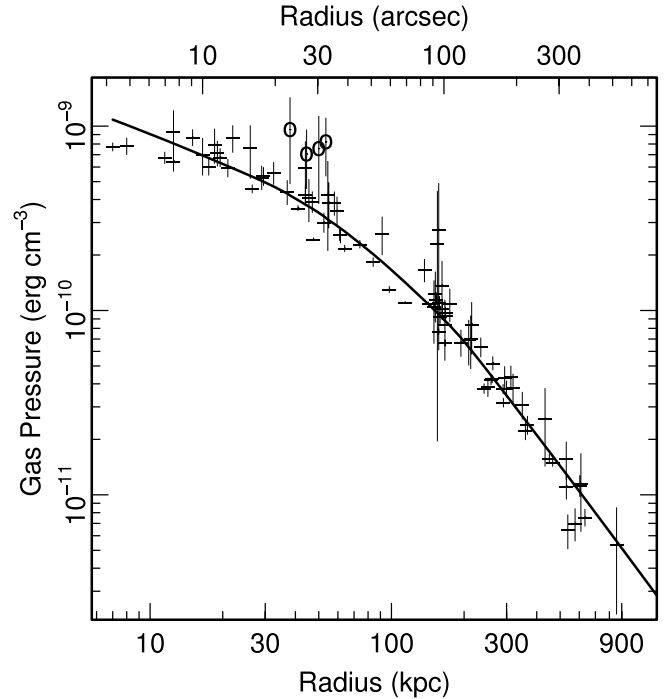

Fig. 14.—Pressure profile from the spectral-mapping deprojection, with a smoothed curve (*solid line*; see text for details). The hot spots are plotted as circles. The x-axis error bars have been omitted for clarity.

thermal energy contained in all four hot spots combined is $(3 \pm 1) \times 10^{59}$ ergs. We note that this result depends only weakly on the volume, V, assumed for the hot spots: the energy, $E \propto V\rho$, and $\rho \propto (K/V)^{1/2}$ (eq. [1]), where K is the MEKAL model normalization, which implies $E \propto (KV)^{1/2}$.

The global morphology of A478 exhibits a regular structure, and the *XMM-Newton* hardness temperature map (Fig. 7, *top right*) shows no sign of significant disturbance in the outskirts of the ICM. This, combined with the presence of a well-established cool core, suggests that A478 cannot have experienced a recent merger or significant disturbance, which might account for the existence of the hot spots. It can be seen from Table 4 that the distances from the cluster center and energy excesses are similar for all the hot spots. Furthermore, they appear to be located (see Fig. 7, *top left*) in rough alignment with the (approximately) conical depressions discovered by S03, corresponding to radio lobes emitted from the active nucleus in the central galaxy. These characteristics point to the influence of an event originating in the cluster center. Correspondingly, it is reasonable to associate them with AGN activity.

On the basis that the hot spots share a common origin, we have extracted a combined spectrum from all four regions and fitted it with a single absorbed MEKAL model. In this way we can gain a better understanding of the degree to which the gas has been heated. We obtain a best-fit temperature of $12.1^{+3.4}_{-2.6}$ keV, an abundance of $0.26^{+0.40}_{-0.26}\ Z_\odot$, and absorption of $(2.4^{+0.3}_{-0.2}) \times 10^{21}$ cm^{-2}. However, by fixing the temperature to the ambient value of 5.5 keV (e.g., see the best-fit curve at ∼50 kpc in Fig. 11) and refitting with the other parameters left free to vary, we obtain a change-in-fit statistic of $\Delta\chi^2 = 16.7$, corresponding to 4.1 σ significance.

We stress that the interpretation of this result as evidence for the existence of the hot spots hinges on the validity of associating these four separate regions with each other. It is certainly possible to achieve a similar level of significance by randomly grouping

TABLE 4
Data for the Hot Spots in the Central ICM of A478

Region	Distance[a] (kpc)	Counts[b]	kT (keV)	χ^2/dof	L_X[c] (10^{42} ergs s^{-1})	Volume[d] (10^{68} cm^3)	ΔE[e] (10^{58} ergs)	t_{cool}[f] (yr)
A...	48–59	1054	$12.1^{+2.6}_{-5.0}$	57.65/43	9.3	2.3	11 ± 6	6×10^8
B...	34–42	727	$9.6^{+2.5}_{-4.4}$	28.93/29	6.7	0.9	4.6 ± 4	4×10^8
C...	38–51	1108	$10.3^{+2.7}_{-3.6}$	45.08/45	10	2.6	8.7 ± 6.5	6×10^8
D...	45–55	639	$10.3^{+3.2}_{-4.5}$	25.99/25	5.4	1.2	5.0 ± 4.6	5×10^8

[a] Nearest/farthest distance to hot spot, measured from the cluster center.
[b] Net source counts in the 0.5–7.0 keV band.
[c] Bolometric X-ray luminosity.
[d] Estimated volume of region.
[e] Estimated excess energy in hot spot.
[f] Gas cooling time (E/L_X, using the *total* rather than the excess hot spot energy). All errors are 1 σ.

hot regions arising from purely statistical fluctuations. However, we believe that the location of the hot spots in the cluster core points to an association between them that indicates they are not merely random peaks in the temperature distribution. Specifically, they lie within a narrow annulus centered on the cluster peak, and they are positioned within the range of angles that enclose the roughly conical bipolar cavities excavated by radio lobes from the central AGN.

6.2. AGN Heating?

If the hot spots are indeed the result of AGN activity, we can address the issue of how they may be connected to the cavities seen in the ICM. The fact that the hot spots are located at least 3–4 times farther away from the cluster center implies a different formation mechanism than that which excavated the cavities. In addition, S03 estimate that the minimum energy needed to create these cavities is $\sim 3 \times 10^{58}$ ergs (Bîrzan et al. [2004] estimate $\sim 1.2 \times 10^{58}$ ergs), which is 1/10 of the thermal energy contained in the hot spots. S03 further estimate a cavity age of $\sim 3 \times 10^7$ yr, from the time taken for the bubbles that formed them to rise buoyantly to their observed location. Similarly, Bîrzan et al. estimate a cavity age between 1×10^7 and 3×10^7 yr by considering three different timescales. For comparison, the time taken to reach a distance of 50 kpc at the local sound speed (920 km s^{-1}) is $\sim 5 \times 10^7$ yr, for a mean ambient gas temperature of 5 keV [$c_s = 1480(T_g/10^8$ K$)^{1/2}$ km s^{-1}; Sarazin 1988]. There is no evidence of a bow shock or X-ray emission excess anywhere near these features, which argues against very recent supersonic motion. It is more likely that the hot spots may have been generated in situ, perhaps in a manner similar to radio hot spots located at the shock termination of radio jets, which have been observed at similar distances from the cluster center (e.g., see the recent sample of Hardcastle & Sakelliou 2004).

An estimate of the minimum timescale for heat conduction to erase the hot spots can be obtained by considering the saturated heat flux, given by

$$q_{sat} = 0.4 \left(\frac{2kT_e}{\pi m_e} \right)^{1/2} n_e kT_e \qquad (6)$$

(Cowie & McKee 1977), where m_e is the electron mass. For hot spot A the gas density is 2×10^{-4} cm^3 and its temperature is 12 keV. Assuming a spherical geometry for this region, with a volume of 2.3×10^{68} cm^3 (Table 4), yields a cooling rate of 10^{44} ergs s^{-1}. Thus, it would take $\sim 3 \times 10^7$ yr to lose its excess energy, 10^{59} ergs, via conduction. This is about 1/10 of the likely lifetime of the hot spots, which implies that heat conduction must be suppressed by

a factor of ~ 10 compared to the *Spitzer* rate. Such a decrease in conduction efficiency could easily be achieved by magnetic fields, which have been shown to lead to suppression factors of ~ 5 in a weakly collisional magnetized plasma (Narayan & Medvedev 2001).

The positions of the northern set of three hot spots (Fig. 7) may offer a clue as to the mechanism responsible for their creation. Their spacing is suggestive of a wide jet opening angle, roughly 100°. This is consistent with the slow jet heating scenario of Soker & Pizzolato (2005), which relies on such a wide angle to produce a poorly collimated, massive, and relatively slow outflow. Moreover, the emissivity of the small bubbles in the ICM predicted from this model is too low for them to be detected in X-ray images with existing telescopes, consistent with the hot spots in A478. The Soker & Pizzolato model is similar to the effervescent heating model of Begelman (2001), which also postulates the formation of many small bubbles, which heat the ICM by doing $P\,dV$ work as they expand and rise. A particularly attractive aspect of this scenario is that the heating is smoothly regulated, since gas cooling acts to steepen the ICM pressure profile, thus yielding more energy from the bubbles' expansion so as to balance the cooling. However, this mechanism for heating the ICM would need to be slow enough to avoid disrupting the nearly power-law scaling of entropy with radius seen in Figure 9.

While the interaction of AGNs with the intracluster medium has been well studied in recent simulations (e.g., Rizza et al. 2000; Reynolds et al. 2001; Churazov et al. 2001; Brüggen & Kaiser 2002; Basson & Alexander 2003; Ruszkowski et al. 2004a), the formation of shock-heated blobs of the type seen in A478 does not appear to be a generic feature. However, Clarke et al. (1997) present three-dimensional magnetohydrodynamical simulations of a supersonic jet, which predict the formation of a pair of X-ray excesses, corresponding to shocked ambient gas, at either side of the jet orifice, which itself produces an X-ray cavity of the type seen in A478. The Clarke et al. simulations proceed for $\sim 10^7$ yr, which does not allow enough time to track the full evolution of these excesses. However, it seems probable that the shock-heated gas in these blobs would expand outward and heat the ICM, which could be an important means of transferring AGN mechanical luminosity into gas thermal energy.

Similarly, the more recent simulations of Omma et al. (2004) appear to produce three distinct density enhancements surrounding the head of an AGN outflow, appearing after $\sim 10^8$ yr. However, the jet responsible for these features is only weakly relativistic so may not be capable of heating these blobs at the level observed in A478. Observationally, perhaps the closest analog to the hot
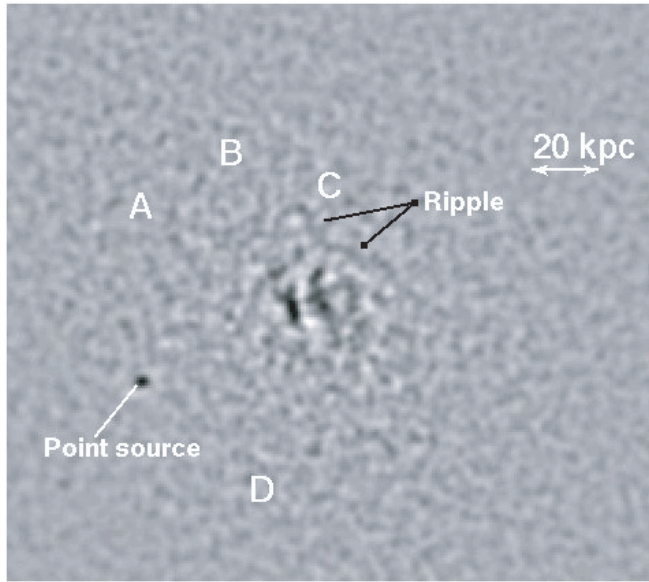
FIG. 15.—Unsharp masked 0.5–7.0 keV *Chandra* image of the core of A478. Each pixel is 0″.492 (0.8 kpc) across, and the image has been smoothed with a Gaussian of $\sigma = 1.5$ pixels. The edges around the radio lobe cavities are clearly visible as an H shape, and there is evidence of a possible curved ripple to the north of the cavities. The positions of the other features are labeled exactly as in Fig. 7.

spots reported here is the heated bubble observed in MKW 3s by Mazzotta et al. (2002). This feature lies at roughly 90 kpc from the cluster core and is approximately 25 kpc in radius in the plane of the sky. More recently, Mazzotta et al. (2004) present new, lower frequency radio observations for this cluster, which show that the radio emission is fully enclosed by the shocked gas. A similar radio–X-ray interaction is observed in Hydra A, where expanding radio lobes, observed at 330 MHz, appear to be driving a shock front (Nulsen et al. 2005). It is possible that equivalent lower frequency observations of A478 may reveal larger radio lobes than those seen in the 1.4 GHz Very Large Array (VLA) map (shown in S03), which might show some evidence of an interaction with the hot spot regions.

However, unlike A478, the MKW 3s bubble is clearly visible as a depression in the surface brightness, and the Hydra A shock front is revealed as a discontinuity in the X-ray image. Similarly, there are spiral armlike features observed by *Chandra* in the elliptical galaxy NGC 4636, produced by weak shocks driven by off-center outbursts (Jones et al. 2002). However, these are ostensibly density enhancements, which produce a clear signature in the surface brightness; as already noted, the hot spots seen in A478 are effectively invisible in X-ray images.

There is further evidence of possible AGN activity disturbing the gas in the form of a tentative ripple in the surface brightness profile of the core (Fig. 15). We have generated an unsharp mask image, using the method of Ruszkowski et al. (2004b), who have simulated viscous dissipation in the ICM caused by AGN activity. A 0.5–7.0 keV raw image was smoothed with a Gaussian kernel of FWHM 6 kpc ($\sigma = 3.1$ pixels) and subtracted from the unsmoothed image; the resulting image has been smoothed with a Gaussian kernel of $\sigma = 1.5$ pixels to highlight the features present. The depressions caused by the radio lobes are clearly seen, producing an H shape that resembles the shape seen in the Ruszkowski et al. (2004b) simulations, and there is also a suggestion of a ripple to the north of the center, lying between 16 and 26 kpc of the AGN. This ripple has a low contrast but is clearly longer and more coherent that the typical noise features in the

image. It is reminiscent of the ripples seen in the ICM of the Perseus (Fabian et al. 2003) and Virgo (at 14 and 17 kpc; Forman et al. 2005) Clusters, which are attributed to shock fronts emanating from the AGN in the central cluster galaxy. If this ripple is genuine, the implied travel time for the feature is roughly 2×10^7 yr (given the assumed local sound speed of 920 km s^{-1} used above), which is comparable to the age of the cavities. We note that the hot spots in A478 are not visible in the unsharp mask image and that they lie at least twice as far out as the putative ripple.

6.3. *Entropy Profile*

The radial variation in gas entropy in A478 (Fig. 9) is unusual in that it appears to follow a broken power-law relation, with an outer logarithmic slope of ~1.1 and a slightly shallower inner slope of ~0.95 within ~0.1 R_{500} but with no indication of a flattening in the core. Non–cool-core clusters generally exhibit a flattening of the entropy profile toward the center (e.g., Rasmussen & Ponman 2004; Pratt & Arnaud 2005), while the effect of cooling is to lower the entropy in exactly this region. It therefore appears to be a conspiracy that causes these two effects to counterbalance each other so as to preserve the scaling evident in the outskirts, where cooling is insignificant. A recent *XMM-Newton* study of 13 nearby cool-core clusters has found that their entropy profiles follow a power law with best-fit logarithmic slope of 0.95 out to roughly half the virial radius (Piffaretti et al. 2005). However, other cool-core clusters show evidence of flattening in their core entropy profile (e.g., Pratt & Arnaud 2003; O'Sullivan et al. 2003; Wise et al. 2004). Moreover, the slope of ~1.1 is predicted to arise from shock-heating due to accretion of gas (Tozzi et al. 2000; Tozzi & Norman 2001), which would not be expected to persist in cooling-dominated cluster cores.

The shape of A478's entropy profile resembles that of the fossil group NGC 6482 ($kT \sim 0.7$ keV), which was the subject of a recent *Chandra* analysis (Khosroshahi et al. 2004). That observation is restricted to the inner 10% of R_{200} of the halo, but it is clear that the entropy data are consistent with a power-law form, with a logarithmic slope slightly shallower than $S \propto r^{1.1}$. Since NGC 6482 is a fossil group, it is expected to be a very old system. However, it shows no evidence for strong cooling and, furthermore, has a gas temperature profile that decreases monotonically with radius, thus ruling out thermal conduction as a means of heating the core. Since NGC 6482 shows some evidence of having a mildly active nucleus, it is possible that this system too has been subjected to a phase of AGN heating that has only recently abated, in which significant gas cooling is currently being reestablished.

Given the apparently significant impact of the AGN on the gas in the core of A478, it is worth noting that excessively large heat input would trigger convective motions that would stir up the gas, flattening the entropy profile and erasing abundance gradients in the core (Churazov et al. 2001, 2002; Brüggen 2002). As there is some enhancement in the metallicity toward the center the ICM (Fig. 2), it is unlikely that a significant disturbance could have occurred recently. This may be because the AGN heating is widely distributed (e.g., effervescent) and thus is not very vigorous. Alternatively, it could indicate that the most unstable (i.e., lowest entropy) gas is also the most metal-rich and that as it cools and moves inward, it produces a central abundance peak.

The cooling time of gas in the center of A478 is only ~9×10^7 yr, roughly 6 times shorter than the cooling time of the hot spots (see Table 4). S03 point out that the observed radio lobes are much smaller than the X-ray cavities, which suggests a fading of the radio source on a timescale of ~10^7–10^8 yr.

Furthermore, the ratio of mechanical power needed to excavate the cavities to the current radio power of the AGN is over 1000 (Bîrzan et al. 2004), by far the largest ratio among the 10 clusters (from their sample of 18 objects) for which they have such data. The inclusion of the hot spot contribution to the energy budget raises this value even higher. Therefore, it is possible that we are witnessing the rapid reestablishment of a cluster cooling flow, following a period of AGN heating of the gas, before the cavities have been completely refilled. On the other hand, an AGN can vary in radio power while its jet power remains constant (Eilek 2004; Bîrzan et al. 2004), and thus some mechanical heating of the ICM may be ongoing, despite the fading radio luminosity, as possibly indicated by the putative ripple seen in Figure 15.

If similar hot spot features are present in other clusters with radio lobe cavities, the timescale on which these features persist as overdense blobs is short enough to make them unlikely to be detected in X-ray images. Furthermore, for much of this time they would reside in close proximity to the cluster center, where emission from the cluster core would be substantial, greatly reducing their surface brightness contrast. The alternative method of detecting them, i.e., locating the hot spots from their temperature signature, is also challenging, since it requires high-resolution hardness mapping and the best possible data quality (the A478 *Chandra* observation analyzed in this work comprises ~400,000 net source counts from the S3 chip).

6.4. *Mass Profile*

The soft core in the mass profile (Fig. 12) of A478 is unusual and apparently at odds with numerical simulations of clusters, which indicate inner logarithmic slopes of -1 (Navarro et al. 1995) or even as steep as -1.5 (Moore et al. 1998). However, such a flat slope is permitted by purely analytical considerations of the dark matter based on fundamental statistical mechanics: Hansen et al. (2005) have recently demonstrated that this approach permits $0 < n < 10/3$ for the index parameter n in equation (5). Furthermore, a number of clusters have been found with similarly flatter cusps in their mass profiles. Tyson et al. (1998) measured a slope of 0.57 ± 0.02, and Sand et al. (2002) observed a value of 0.35 for two different clusters, on the basis of strong-gravitational lensing analyses. More recently, Sand et al. (2004) have studied lensing arcs in six clusters and report a mean slope of 0.52 ± 0.05. It is interesting to note that their sample comprises only clusters with a dominant brightest cluster galaxy, as is the case for A478. Also, the cluster Abell 1795 has been shown to have an inner mass profile logarithmic slope of $0.59^{+0.12}_{-0.17}$ (90% confidence), inferred from a *Chandra* analysis (Ettori et al. 2002).

It must be remembered that, unlike lensing measurements, our X-ray analysis hinges on the assumption of hydrostatic equilibrium, which could easily break down in the core, given the impact of the central AGN. For example, the presence of significant nonthermal pressure support could mimic a less concentrated mass distribution. The simulations of Faltenbacher et al. (2005) indicate that random bulk motions of gas account for 10% of the total pressure support in clusters. Also, a recent *XMM-Newton* analysis of the spectrum of pressure fluctuations in the Coma Cluster found a lower limit of ~10% for the contribution to the ICM pressure support arising from turbulence. It is possible that bulk

or turbulent motion of gas associated with AGN activity could be significant in the core of A478. Presumably, such a mechanism would give rise to a radially diminishing pressure contribution, which could act to flatten the inferred mass distribution in the manner observed. In such a situation, the inferred gas fraction would be increasingly overestimated at smaller radii, which may explain the radially decreasing trend observed within ~200 kpc in Figure 13.

7. CONCLUSIONS

We have studied the detailed thermodynamic properties of the intracluster medium in the relaxed, cool-core cluster Abell 478, using *Chandra* and *XMM-Newton* X-ray data. Our main findings can be summarized as follows:

1. We find that our *Chandra* X-ray temperature measurements are systematically hotter than those from *XMM-Newton*, as also reported by Pointecouteau et al. (2004). By selecting approximately isothermal regions, we find slightly better agreement between the two. However, by simulating multiphase spectra and fitting them with a single-temperature model, we find no evidence for significant disagreement between *Chandra* and *XMM-Newton*. We therefore conclude that the observed discrepancy cannot be fully attributed to nonisothermality in fitting single-temperature models.

2. The entropy profile appears to agree well with the empirical modified entropy scaling of Ponman et al. (2003). Moreover, the power-law trend continues to the innermost radius measured (<10 kpc), with only a slightly shallower slope. There is no evidence of any core in the entropy profile.

3. Under the assumption of hydrostatic equilibrium, we infer a mass profile that exhibits a soft core, characterized by a logarithmic slope of -0.35 ± 0.22. This is significantly flatter than an NFW profile (slope of -1) but is consistent with the recent gravitational lensing results of Sand et al. (2004) for clusters containing a dominant central galaxy.

4. We have discovered four hot spots in the ICM located well within the cool core, where the gas is roughly twice as hot as its surroundings. The combined excess energy associated with these regions is $(3 \pm 1) \times 10^{59}$ ergs, which is ~10 times the energy needed to excavate the cavities produced by radio lobes from the central AGN. The properties of these hot spots suggest they may the result of strong-shock heating from a jet or outflow originating in the AGN.

REFERENCES

Afshordi, N., Lin, Y., & Sanderson, A. J. R. 2005, ApJ, 629, 1
Allen, S. W., Schmidt, R. W., Fabian, A. C., & Ebeling, H. 2003, MNRAS, 342, 287
Anders, E., & Grevesse, N. 1989, Geochim. Cosmochim. Acta, 53, 197
Arnaud, M., & Evrard, A. E. 1999, MNRAS, 305, 631

Basson, J. F., & Alexander, P. 2003, MNRAS, 339, 353
Begelman, M. C. 2001, in ASP Conf. Ser. 240, Gas and Galaxy Evolution, ed. J. E. Hibbard, M. P. Rupen, & J. H. van Gorkom (San Francisco: ASP), 363
Bîrzan, L., Rafferty, D. A., McNamara, B. R., Wise, M. W., & Nulsen, P. E. J. 2004, ApJ, 607, 800

Böhringer, H., Matsushita, K., Churazov, E., Ikebe, Y., & Chen, Y. 2002, A&A, 382, 804
Brüggen, M. 2002, ApJ, 571, L13
Brüggen, M., & Kaiser, C. R. 2002, Nature, 418, 301
Burns, J. O. 1990, AJ, 99, 14
Churazov, E., Brüggen, M., Kaiser, C. R., Böhringer, H., & Forman, W. 2001, ApJ, 554, 261
Churazov, E., Sunyaev, R., Forman, W., & Böhringer, H. 2002, MNRAS, 332, 729
Clarke, D. A., Harris, D. E., & Carilli, C. L. 1997, MNRAS, 284, 981
Cowie, L. L., & McKee, C. F. 1977, ApJ, 211, 135
Croston, J. H., Hardcastle, M. J., & Birkinshaw, M. 2005, MNRAS, 357, 279
David, L. P., Jones, C., & Forman, W. 1995, ApJ, 445, 578
de Plaa, J., Kaastra, J. S., Tamura, T., Pointecouteau, E., Mendez, M., & Peterson, J. R. 2004, A&A, 423, 49
Dickey, J. M., & Lockman, F. J. 1990, ARA&A, 28, 215
Edge, A. C., & Stewart, G. C. 1991, MNRAS, 252, 414
Eilek, J. A. 2004, in The Riddle of Cooling Flows in Galaxies and Clusters of Galaxies, ed. T. Reiprich, J. Kempner, & N. Soker (Charlottesville: Univ. Virginia), http://www.astro.virginia.edu/coolflow
Ettori, S., Fabian, A. C., Allen, S. W., & Johnstone, R. M. 2002, MNRAS, 331, 635
Fabian, A. C., Sanders, J. S., Allen, S. W., Crawford, C. S., Iwasawa, K., Johnstone, R. M., Schmidt, R. W., & Taylor, G. B. 2003, MNRAS, 344, L43
Fabian, A. C., et al. 2000, MNRAS, 318, L65
Fabricant, D., Lecar, M., & Gorenstein, P. 1980, ApJ, 241, 552
Fairley, B. W., Jones, L. R., Scharf, C., Ebeling, H., Perlman, E., Horner, D., Wegner, G., & Malkan, M. 2000, MNRAS, 315, 669
Faltenbacher, A., Kravtsov, A. V., Nagai, D., & Gottlöber, S. 2005, MNRAS, 358, 139
Finoguenov, A., Henriksen, M. J., Briel, U. G., de Plaa, J., & Kaastra, J. S. 2004a, ApJ, 611, 811
Finoguenov, A., Pietsch, W., Aschenbach, B., & Miniati, F. 2004b, A&A, 415, 415
Forman, W., et al. 2005, ApJ, in press (astro-ph/0312576)
Fujita, Y., Suzuki, T. K., & Wada, K. 2004, ApJ, 600, 650
Gardini, A., & Ricker, P. M. 2004, Mod. Phys. Lett. A, 19(31), 2317
Garilli, B., Bottini, D., Maccagni, D., Carrasco, L., & Recillas, E. 1996, ApJS, 105, 191
Hansen, S. H., Egli, D., Hollenstein, L., & Salzmann, C. 2005, NewA, 10, 379
Hardcastle, M. J., & Sakelliou, I. 2004, MNRAS, 349, 560
Henry, J. P., Finoguenov, A., & Briel, U. G. 2004, ApJ, 615, 181
Jones, C., Forman, W., Vikhlinin, A., Markevitch, M., David, L., Warmflash, A., Murray, S., & Nulsen, P. E. J. 2002, ApJ, 567, L115
Kaastra, J. S., et al. 2004, A&A, 413, 415
Khosroshahi, H. G., Jones, L. R., & Ponman, T. J. 2004, MNRAS, 349, 1240
Kim, W., & Narayan, R. 2003, ApJ, 596, 889
Lewis, A. D., Buote, D. A., & Stocke, J. T. 2003, ApJ, 586, 135
Lockman, F. J. 2005, in Soft X-Ray Emission from Clusters of Galaxies and Related Phenomena, ed. R. Lieu & J. Mittaz (Berlin: Springer)
Lumb, D. H., Finoguenov, A., Saxton, R., Aschenbach, B., Gondoin, P., Kirsch, M., & Stewart, I. M. 2003, Proc. SPIE, 4851, 255
Makishima, K., et al. 2001, PASJ, 53, 401
Mazzotta, P., Brunetti, G., Giacintucci, S., Venturi, T., & Bardelli, S. 2004, J. Korean Astron. Soc., 37, 381
Mazzotta, P., Kaastra, J. S., Paerels, F. B., Ferrigno, C., Colafrancesco, S., Mewe, R., & Forman, W. R. 2002, ApJ, 567, L37

McLaughlin, D. E. 1999, AJ, 117, 2398
McNamara, B. R., et al. 2001, ApJ, 562, L149
Mohr, J. J., & Evrard, A. E. 1997, ApJ, 491, 38
Mohr, J. J., Mathieson, B., & Evrard, A. E. 1999, ApJ, 517, 627
Moore, B., Governato, F., Quinn, T., Stadel, J., & Lake, G. 1998, ApJ, 499, L5
Narayan, R., & Medvedev, M. V. 2001, ApJ, 562, L129
Navarro, J. F., Frenk, C. S., & White, S. D. M. 1995, MNRAS, 275, 720
Nulsen, P. E. J., McNamara, B. R., Wise, M. W., & David, L. P. 2005, ApJ, 628, 629
Omma, H., Binney, J., Bryan, G., & Slyz, A. 2004, MNRAS, 348, 1105
Osmond, J. P. F., & Ponman, T. J. 2004, MNRAS, 350, 1511
O'Sullivan, E., Vrtilek, J. M., Read, A. M., David, L. P., & Ponman, T. J. 2003, MNRAS, 346, 525
Paturel, G., et al. 1997, A&AS, 124, 109
Peterson, J. R., Kahn, S. M., Paerels, F. B. S., Kaastra, J. S., Tamura, T., Bleeker, J. A. M., Ferrigno, C., & Jernigan, J. G. 2003, ApJ, 590, 207
Piffaretti, R., Jetzer, P., Kaastra, J. S., & Tamura, T. 2005, A&A, 433, 101
Pointecouteau, E., Arnaud, M., Kaastra, J., & de Plaa, J. 2004, A&A, 423, 33
Ponman, T. J., Cannon, D. B., & Navarro, J. F. 1999, Nature, 397, 135
Ponman, T. J., Sanderson, A. J. R., & Finoguenov, A. 2003, MNRAS, 343, 331
Pratt, G. W., & Arnaud, M. 2003, A&A, 408, 1
———. 2005, A&A, 429, 791
Rasmussen, J., & Ponman, T. J. 2004, MNRAS, 349, 722
R Development Core Team. 2005, R: A Language and Environment for Statistical Computing (Vienna: R Foundation for Statistical Computing)
Reynolds, C. S., Heinz, S., & Begelman, M. C. 2001, ApJ, 549, L179
Rizza, E., Loken, C., Bliton, M., Roettiger, K., Burns, J. O., & Owen, F. N. 2000, AJ, 119, 21
Ruszkowski, M., Brüggen, M., & Begelman, M. C. 2004a, ApJ, 611, 158
———. 2004b, ApJ, 615, 675
Sand, D. J., Treu, T., & Ellis, R. S. 2002, ApJ, 574, L129
Sand, D. J., Treu, T., Smith, G. P., & Ellis, R. S. 2004, ApJ, 604, 88
Sanderson, A. J. R., Ponman, T. J., Finoguenov, A., Lloyd-Davies, E. J., & Markevitch, M. 2003, MNRAS, 340, 989
Sarazin, C. L. 1988, X-Ray Emission from Clusters of Galaxies (Cambridge: Cambridge Univ. Press)
Schmidt, R. W., Allen, S. W., & Fabian, A. C. 2004, MNRAS, 352, 1413
Soker, N., & Pizzolato, F. 2005, ApJ, 622, 847
Struble, M. F., & Rood, H. J. 1999, ApJS, 125, 35
Strüder, L., et al. 2001, A&A, 365, L18
Sun, M., Jones, C., Murray, S. S., Allen, S. W., Fabian, A. C., & Edge, A. C. 2003, ApJ, 587, 619 (S03)
Tamura, T., et al. 2001, A&A, 365, L87
Tozzi, P., & Norman, C. 2001, ApJ, 546, 63
Tozzi, P., Scharf, C., & Norman, C. 2000, ApJ, 542, 106
Tyson, J. A., Kochanski, G. P., & dell'Antonio, I. P. 1998, ApJ, 498, L107
Vikhlinin, A., Markevitch, M., Murray, S. S., Jones, C., Forman, W., & Van Speybroeck, L. 2005, ApJ, 628, 655
Vikhlinin, A., McNamara, B. R., Forman, W., Jones, C., Quintana, H., & Hornstrup, A. 1998, ApJ, 502, 558
Voigt, L. M., & Fabian, A. C. 2004, MNRAS, 347, 1130
Voit, G. M., & Ponman, T. J. 2003, ApJ, 594, L75
Wise, M. W., McNamara, B. R., & Murray, S. S. 2004, ApJ, 601, 184
Zhang, Y.-Y., Finoguenov, A., Böhringer, H., Ikebe, Y., Matsushita, K., & Schuecker, P. 2004, A&A, 413, 49
Zhao, H. 1996, MNRAS, 278, 488